

## Electronic supplementary information

### Unveiling the role of surface, shape and defects for theranostic applications of iron oxide nanoparticles

Geoffrey Cotin<sup>1,2</sup>, Cristina Blanco-Andujar<sup>1</sup>, Francis Perton<sup>1</sup>, Laura Asín<sup>3</sup>, Jesus M. de la Fuente<sup>3</sup>, Wilfried Reichardt<sup>4,5,6</sup>, Denise Schaffner<sup>4</sup>, Dinh-Vu Ngyen<sup>1</sup>, Damien Mertz<sup>1</sup>, Céline Kiefer<sup>1</sup>, Florent Meyer<sup>7</sup>, Simo Spassov<sup>8</sup>, Ovidiu Ersen<sup>1</sup>, Michael Chatzidakis<sup>9</sup>, Gianluigi A. Botton<sup>9</sup>, Céline Hénoumont<sup>10</sup>, Sophie Laurent<sup>10</sup>, Jean-Marc Greneche<sup>11</sup>, Francisco J. Teran<sup>12,13</sup>, Daniel Ortega<sup>12,14,15</sup>, Delphine Felder-Flesch<sup>1</sup>, Sylvie Begin-Colin<sup>1,2,\*</sup>

<sup>1</sup> Université de Strasbourg, CNRS, Institut de Physique et Chimie des Matériaux de Strasbourg, UMR 7504, F-67034 Strasbourg, France

<sup>2</sup> Labex CSC, Fondation IcFRC/Université de Strasbourg, 8 allée Gaspard Monge BP 70028 F - 67083 Strasbourg Cedex.

<sup>3</sup> Instituto de Nanociencia y Materiales de Aragón (INMA) CSIC-Universidad de Zaragoza & Centro de Investigación Biomédica en Red de Bioingeniería, Biomateriales y Nanomedicina (CIBER-BBN), 50018 Zaragoza, Spain

<sup>4</sup> Department of Radiology, Medical Physics, Medical Center, University of Freiburg, Faculty of Medicine, University of Freiburg, Germany

<sup>5</sup> German Cancer Consortium (DKTK), Heidelberg, Germany

<sup>6</sup> German Cancer Research Center (DKFZ), Heidelberg, Germany

<sup>7</sup> Université de Strasbourg, INSERM, UMR 1121 Biomaterials and Bioengineering, FMFS, F-67000 Strasbourg, France

<sup>8</sup> Centre de Physique du Globe de l'Institut Royal Météorologique de Belgique

<sup>9</sup> Dept of Materials Science and Engineering, McMaster University, 1280 Main Street West, Hamilton, Ontario, Canada, L8S 4M1

<sup>10</sup> Université de Mons, General, Organic and Biomedical Chemistry Unit, NMR and Molecular Imaging Laboratory, 7000 Mons, Belgium

<sup>11</sup> Institut des Molécules et Matériaux du Mans IMMM UMR CNRS 6283, Université du Maine, Avenue Olivier Messiaen, 72085 Le Mans Cedex 9, France

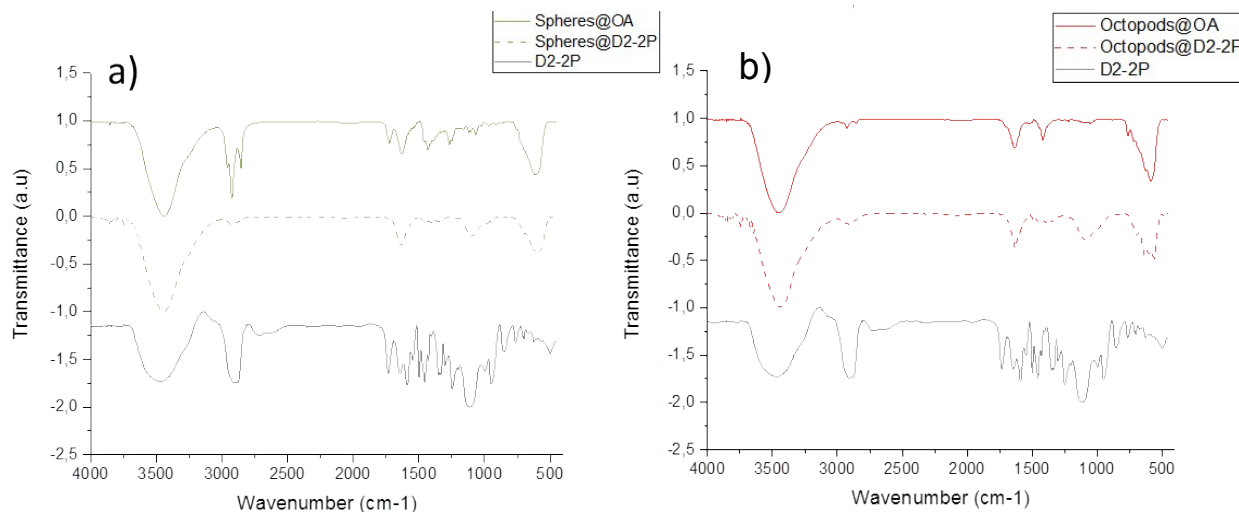
<sup>12</sup> iMdea Nanociencia, Campus Universitario de Cantoblanco, 28049 Madrid, Spain

<sup>13</sup> Nanobiotecnología (iMdea-Nanociencia), Unidad Asociada al Centro Nacional de Biotecnología (CSIC), 28049 Madrid, Spain

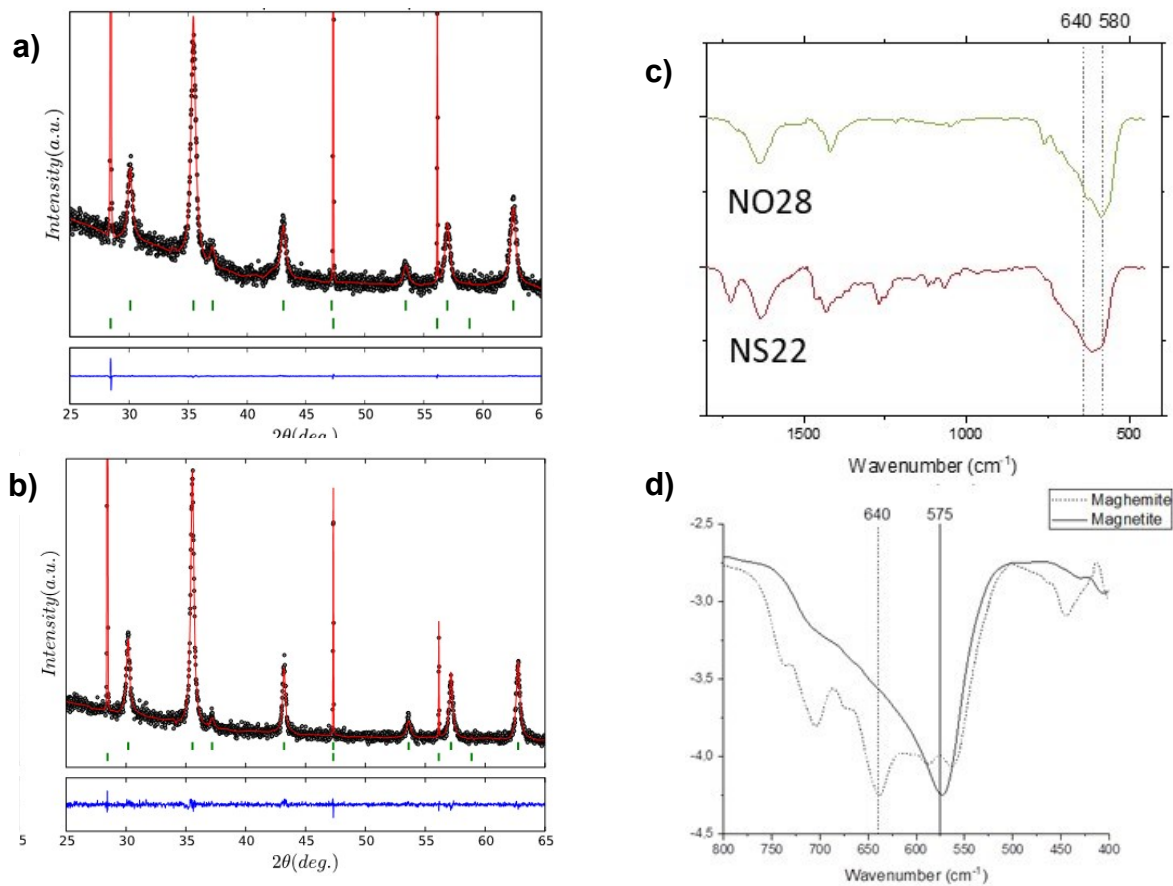
<sup>14</sup> Condensed Matter Physics Department, Faculty of Sciences, University of Cádiz, 11510 Puerto Real, Spain

<sup>15</sup> Institute of Research and Innovation in Biomedical Sciences of the Province of Cádiz (INiBICA), 11009 Cádiz, Spain

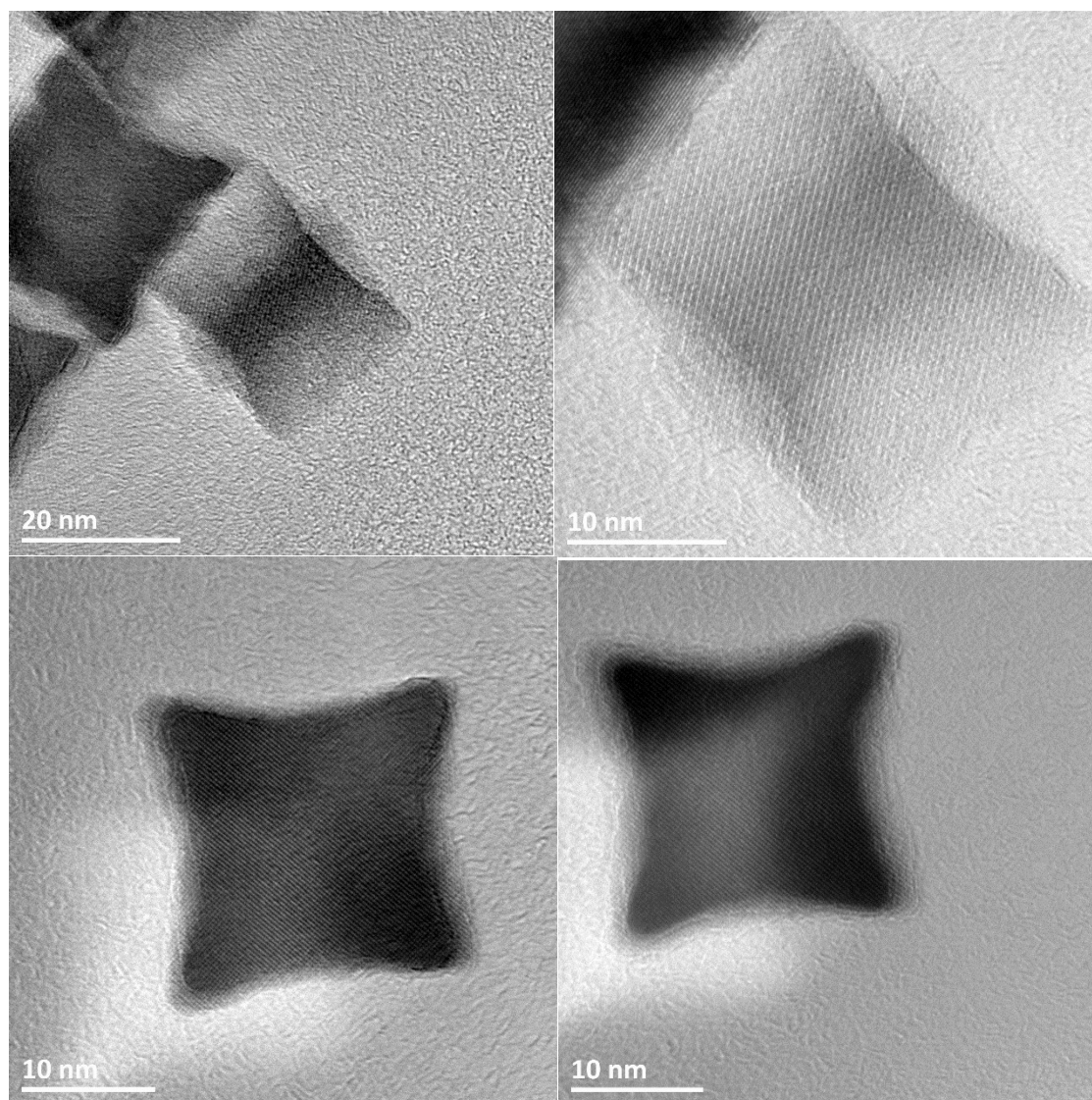
**Validation by IR spectroscopy of the dendron grafting.** The IR spectra of the NP after grafting (NP@D2-2P) are compared to the one after synthesis (NP@OA) and the one of the D2-2P molecules (Figure S1). “Spheres” corresponds to NS22 and “octopods” to NO28. The IR spectrum of the D2-2P molecule presented various P-O bands with a P=O band appearing at  $1200\text{ cm}^{-1}$  and P-OH bands at  $1027$  and  $995\text{ cm}^{-1}$ <sup>1-4</sup>. An intense C-O-C band is detected at  $1110\text{ cm}^{-1}$  and the C=O band appears at  $1700\text{ cm}^{-1}$ . After the grafting step, the carboxylate bands observed on the NP@OA at around  $1500$  and  $1400\text{ cm}^{-1}$  are replaced with the C=O band of the D2-2P at  $1700\text{ cm}^{-1}$  and N-CO at  $1640\text{ cm}^{-1}$ . The alkyl chain bands at  $2900$  and  $2800\text{ cm}^{-1}$  have almost completely disappeared. The C-O-C and the P=O bands are not observed such as P-OH bands due to the formation of the P-O-Fe ( $992\text{ cm}^{-1}$ ) bonds<sup>3</sup>. The disappearance of the three bands indicated a strong coordination of the dendron at the NPs surface. The weak band at  $716\text{ cm}^{-1}$  from the precursor still observed before dendronisation is not seen after.



**Figure S1.** FTIR spectra of the NPs before (NP@OA, plain) and after (NP@D2-2P, dashed) grafting and of the D2-2P dendron (gray) for a) NS22 and b) NO28

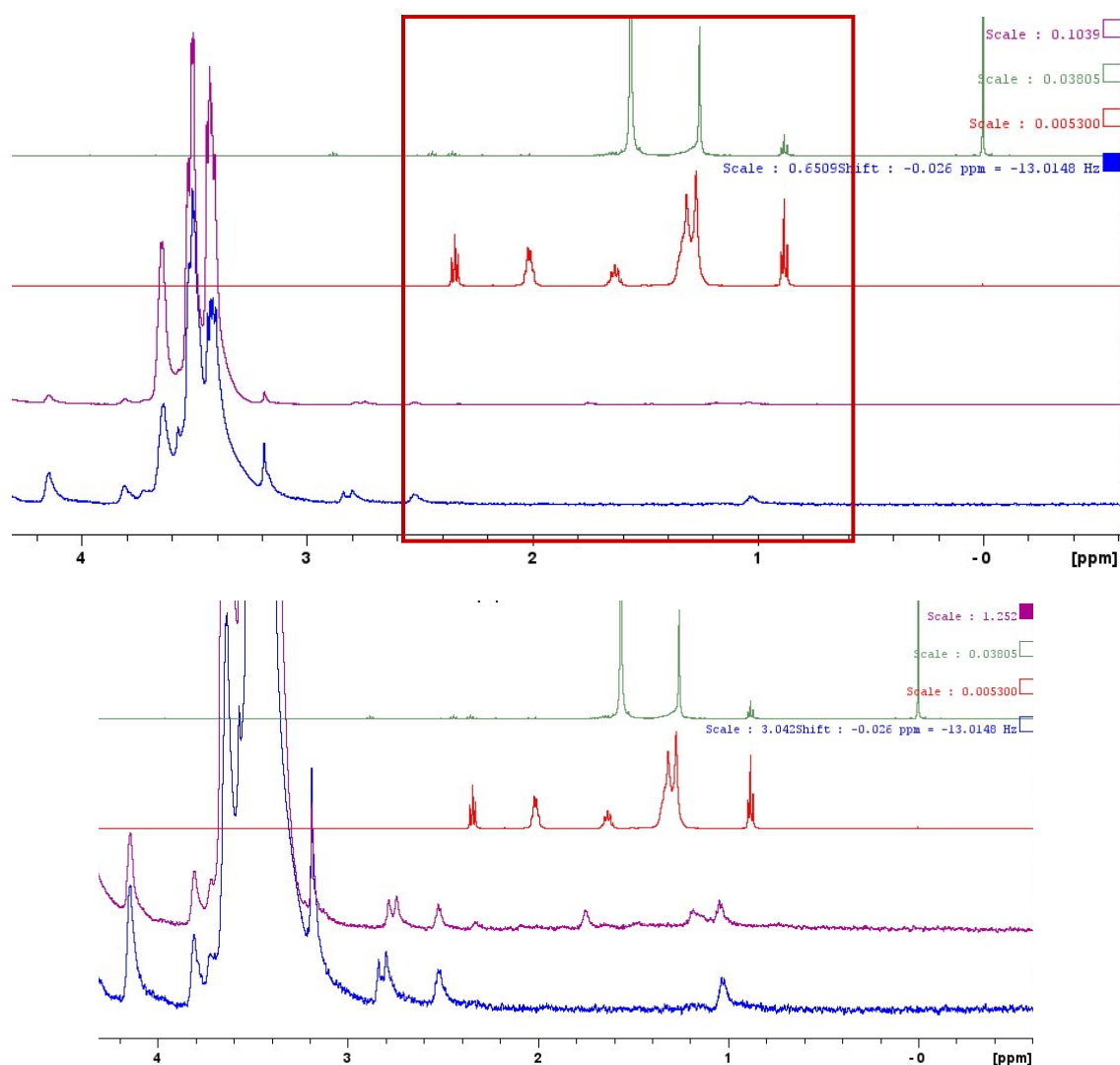


**Figure S2.** XRD refinement of NS22 a), NO28 b) (sharp peaks are attributed to high-purity silicon powder ( $a = 0.543\ 082\ \text{nm}$ ) used as an internal standard), IR spectra of NS22 (red) and NO28 (green) c) and typical IR spectra of oxidized magnetite and maghemite d).

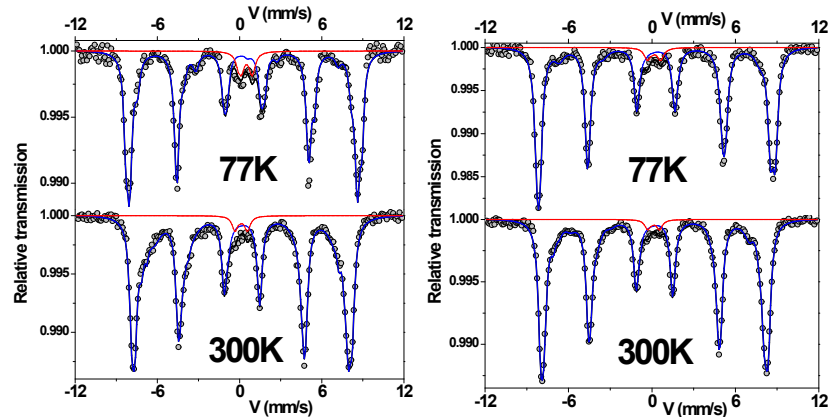


**Figure S3.** HRTEM images of NO18 nanoparticles

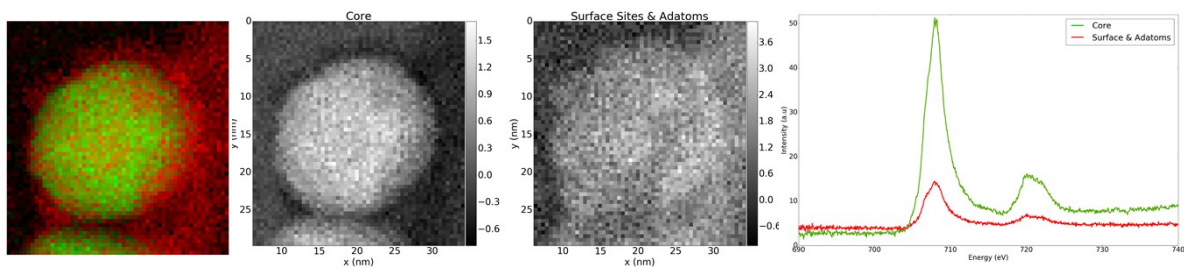
**High Resolution-Magic Angle Spinning (HR-MAS) measurements.** This method is used in solid state NMR spectroscopy and consists in performing NMR measurement by spinning the sample at the magic angle (about  $54.74^\circ$ ) with respect to the magnetic field orientation. This allows to narrow the signal usually broadened by the presence of magnetic atoms. The HR-MAS NMR spectra (Figures S3) evidenced the presence of the dendritic molecules on the surface of the NPs, whatever their shape. However, very weak supplementary peaks were observed in the range 0.9 -2.5 ppm, which were attributed to free stearate or oleic acid. The peaks are shifted in the presence of the NPs but this is an artefact due to the structure of the solvent<sup>5</sup> as alkyl chains are probably not fully extended in  $D_2O$  which is much more polar than  $CDCl_3$ . The weak intensity of the stearate / oleic acid signal indicated that only traces were present on the surface of the NPs.



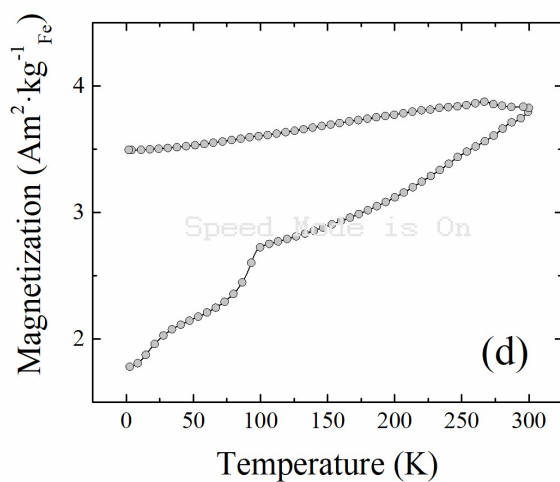
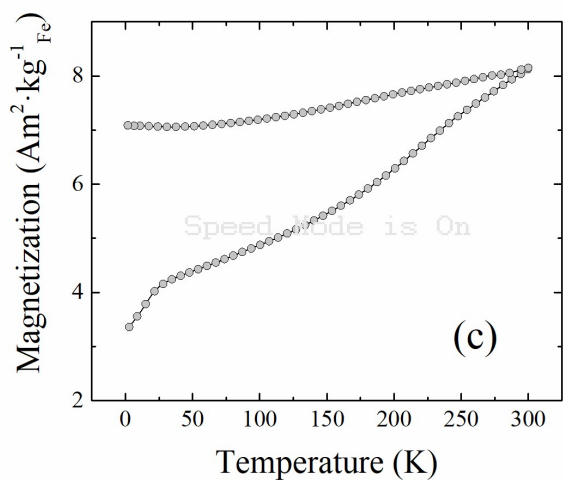
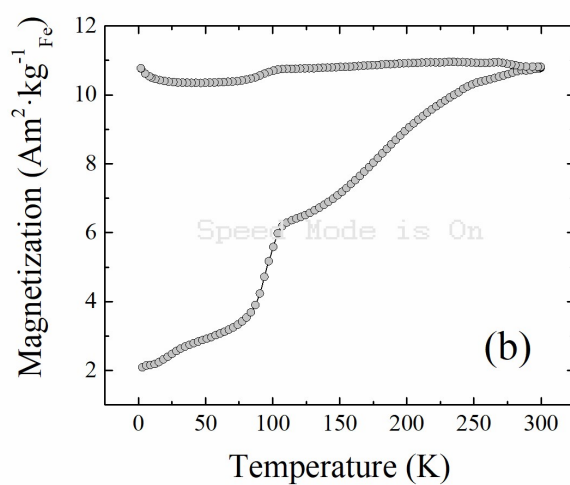
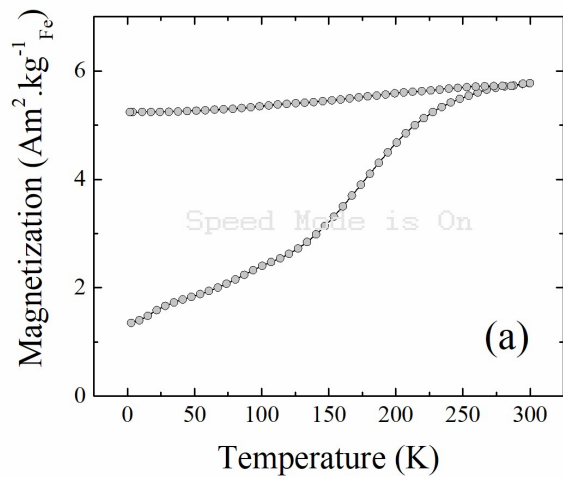
**Figure S4.** TOP:  $^1\text{H}$  HR-MAS spectra of NS22 (purple), compared to  $^1\text{H}$  NMR spectra of the dendron molecule in  $\text{D}_2\text{O}$  (blue), NaSt in  $\text{CDCl}_3$  (red) and OA in  $\text{CDCl}_3$  (green). BOTTOM: Enlargement of the top figure.



**Figure S5.** Mössbauer spectra at 300 and 77K of nanospheres (NS22) (left), octopods (NO18) (right)



**Figure S6.** EELS analysis of sample NS22. EELS signals corresponding to the core and the surface of NPs extracted using independent component analysis (ICA). The residual contributions contain the signal from the ligand molecules around the NPs.



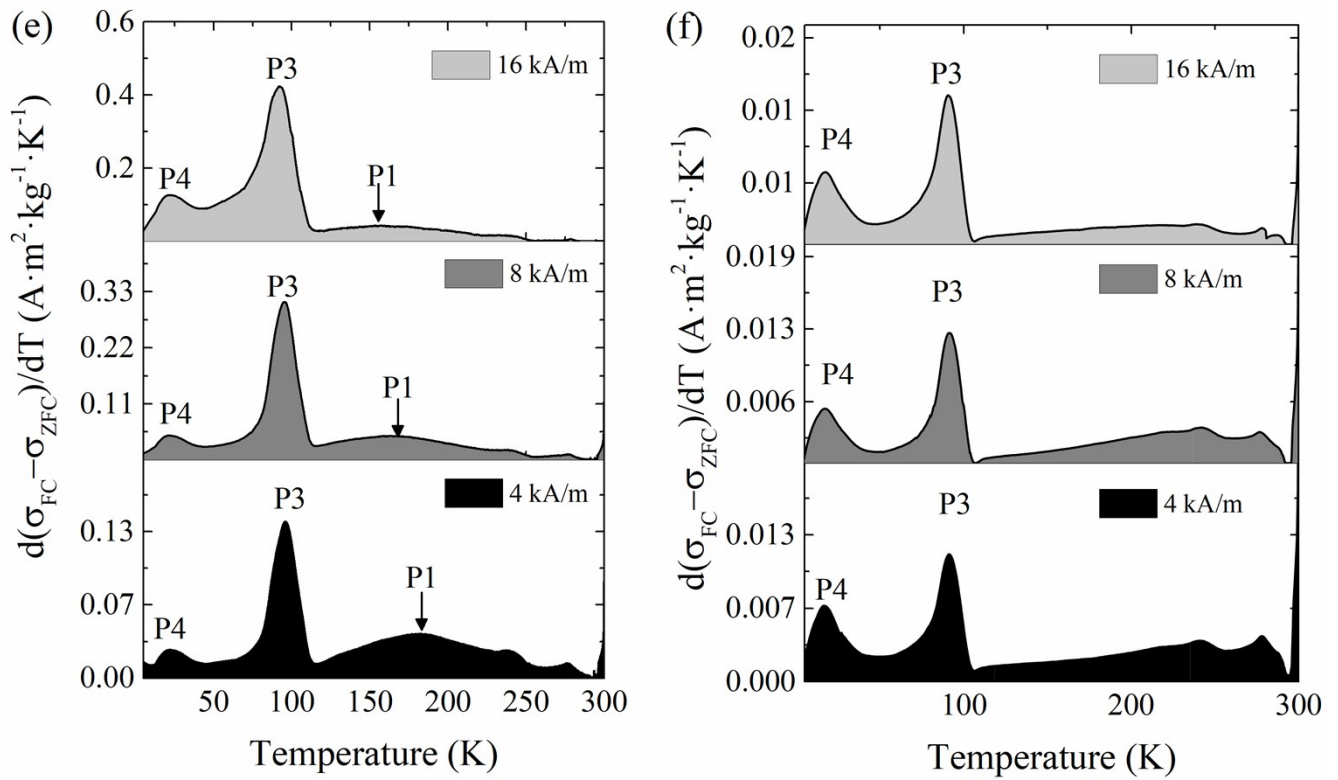


**Figure S7.** ZFC/FC curves under  $4 \text{ kA}\cdot\text{m}^{-1}$  (ZFC curve – red, FC curve blue) For samples a) NS18 b) NS22, c) NO18 d) NO28. Differential ZFC magnetization curves with respect to the temperature for samples e) NS22 and f) NO28 obtained at external fields of 4, 8 and  $16 \text{ kA}\cdot\text{m}^{-1}$ .

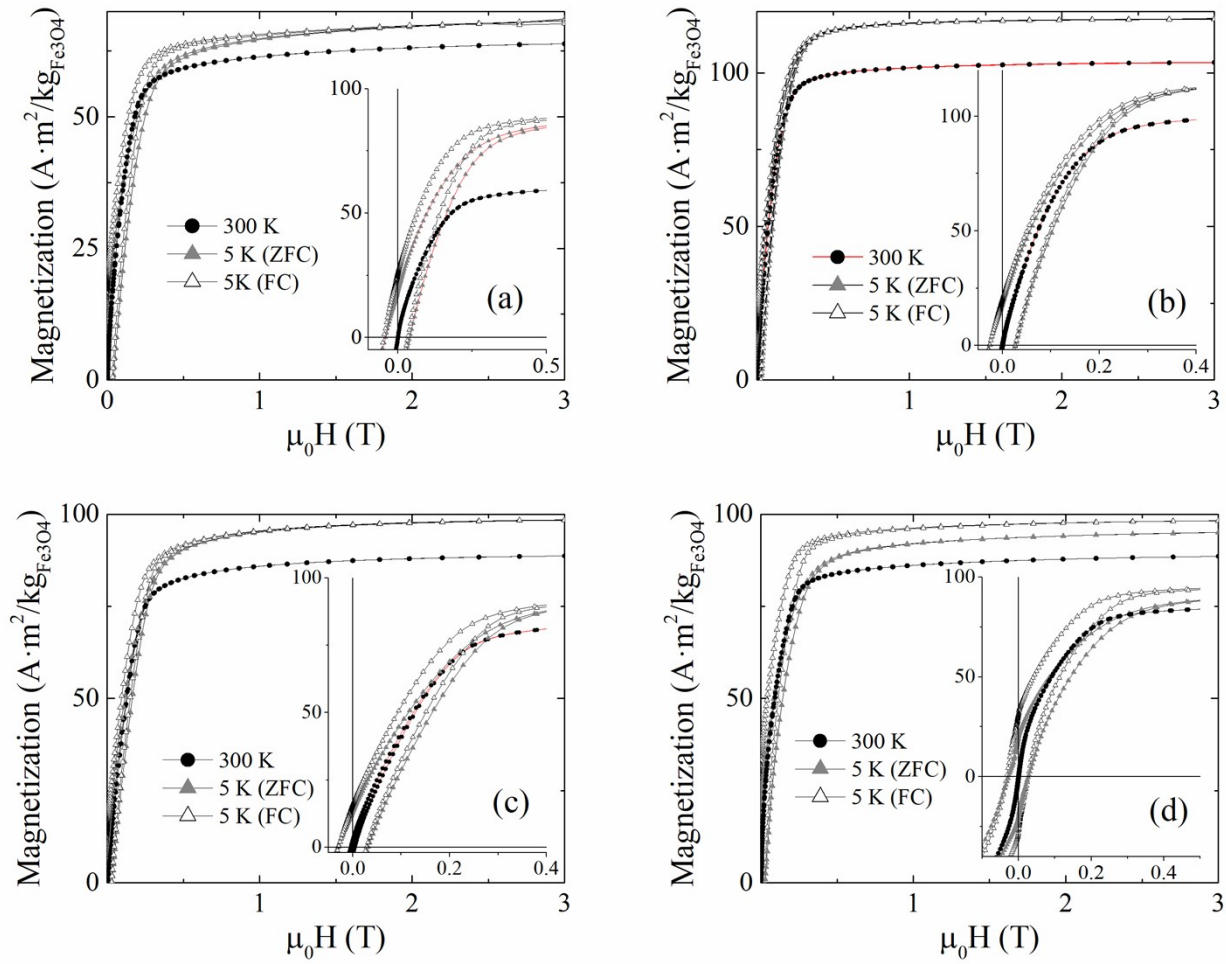


**Figure S8.** ZFC hysteresis curves measured at 300 and 5 K, and FC hysteresis loop at 5 K measured at  $\mu_0 H = 3T$  for samples (a) NS18, (b) NO18, (c) NS28 and (d) NS22.

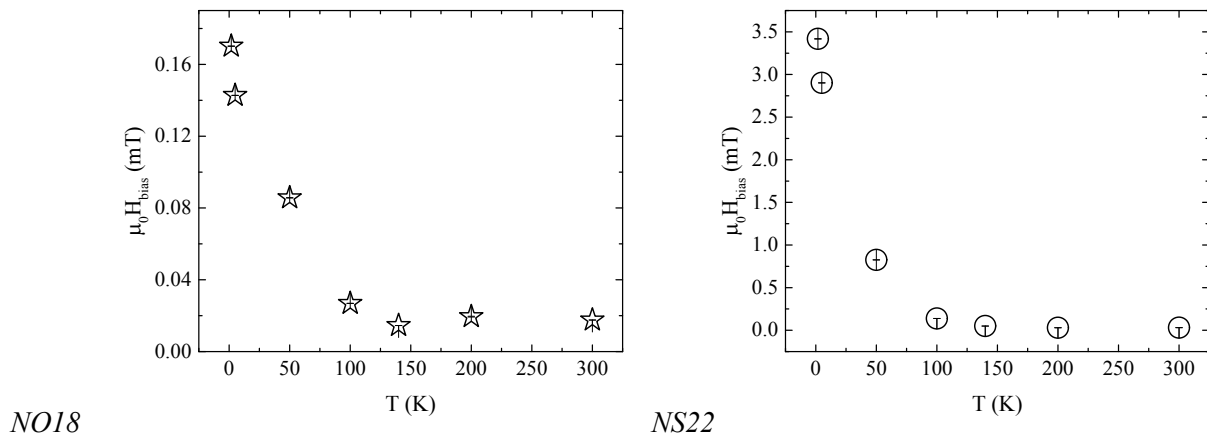


**Figure S9.** Temperature dependence of the exchange bias ( $H_{bias}$ ) effect for NO18 and NS22

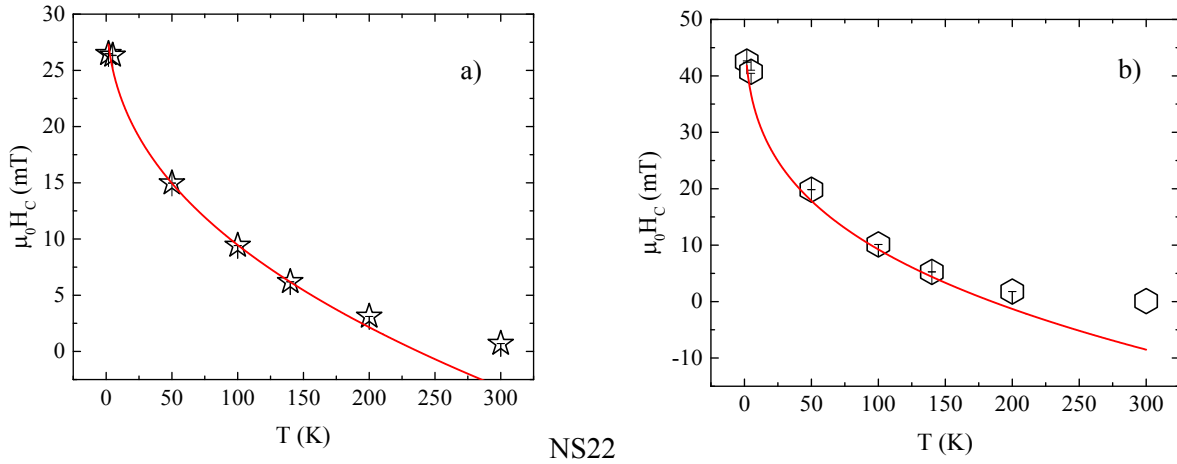


**Figure S10.** Temperature dependence of  $\mu_0 H_C$  for samples NO18 (a), NS22 (b), showing the fit to Eq. 2 (continuous line).

For non-interacting nanoparticles, the relationship between  $H_c$  and particle size is given by:

$$H \cdot H_{c0}^{-1} = 1 - (d_{SPM}/d)^{1/2} \quad \text{Eq. 1}$$

where  $d_{SPM}$  is the particle size associated to the superparamagnetic threshold, and  $H_{c0}$  is the value to which  $H_c$  tends to decrease when the particle size  $d$  tends to  $d_{SPM}$ . NPs with a diameter equal to  $D_{SPM}$  do not present coercivity when temperature has reached the blocking temperature ( $T_B$ ), as stated by the Kneller equation:

$$H \cdot H_{c0}^{-1} = 1 - (T/T_B)^\beta, \text{ or } H = H_{c0} - (H_{c0}/T_B^\beta) T^\beta \quad \text{Eq. 2}$$

Where the factor  $\beta$  originally equals 0.5. As seen for other fine particle systems<sup>6</sup>, none of the samples do fit to Eq. 2. The main disagreement comes from the exponent  $\beta$ , which in most of the studied samples is 0.3 upon fitting the experimental data to Eq. 2. This discrepancy is due to the unavoidable existence of a size distribution in all NPs and the equivalent  $T_B$  distribution.  $\beta$  values are such that allow to obtain reasonable values of  $H_{c0}$  and  $T_B$  that are also consistent with those extracted from ZFC/FC curves.

**Table S1.** Results from fitting the temperature evolution of coercivity to a modified Kneller relationship (Eq. 2) for samples NS22, NO18.

Sample	$H_{c0}$ (mT)	$T_B$ (K)	$\beta$
NS22	56.6	185.3	0.3
NO18	31.0	237.1	0.3

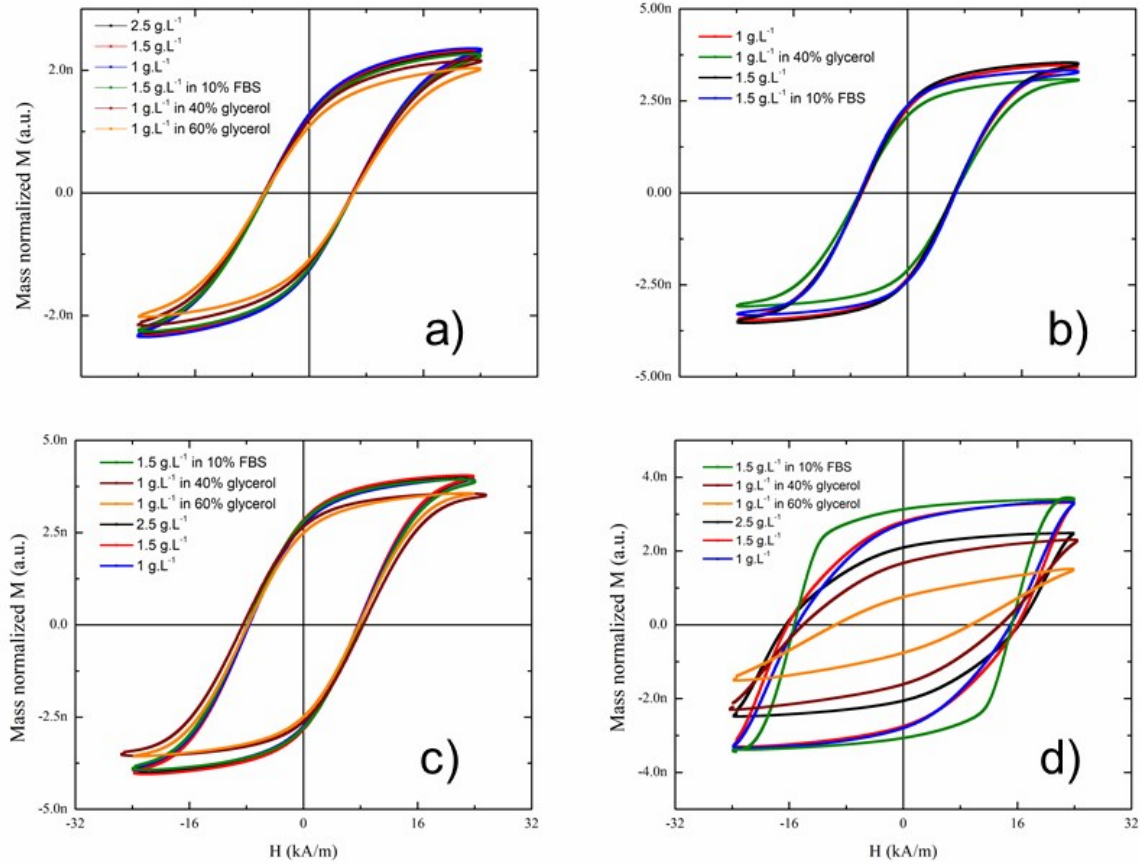


**Figure S11.** Magnetization curves of dendronized a) NS18, b) NS22, c) NO18 and d) NO28 at 96 kHz as a function of concentrations and different media tuning the viscosity.

## Assessment of the effective anisotropy

### 1. Assessment of shape anisotropy

The shape anisotropy of a spherical particle is determined by the difference of the oblate and prolate demagnetization factors  $N_b$  and  $N_a$ , respectively, *i.e.*  $N_b - N_a$  depending both on the width length ratio. Considering uniaxial anisotropy, the shape anisotropy constant is calculated as follows:

$$K_{us} = \frac{1}{2} \mu_0 (N_b - N_a) M_s^2$$

For perfect cubes and spheres the difference is zero. Thus, a uniform cube has no shape anisotropy. Neglecting the shape effect of the edges and approximating the cuboid as an ellipsoid, the different  $N_b$  and  $N_a$  can be found in the Figure 4.5 of ref. <sup>7</sup>. The anisotropy constant is then calculated as follows:

$$K_{us} = \frac{1}{2} 4\pi \cdot 10^{-7} (0.3869 - 0.2773) (480 \cdot 10^3)^2 \frac{V_s}{Am} \frac{A^2}{m^2}$$

$$K_{us} = 15866 \frac{V_s}{m} \frac{A}{m^2} = 15866 \frac{J}{m^3}$$

The differences between a nearly spherical ellipsoid and a cuboid of the same dimensions should not be so big<sup>8</sup>. This makes clear that the surface and uniaxial shape anisotropy are of equal importance.

### 2. Crystalline anisotropy

Here one can take a literature value. Figure 3-7 in <sup>7</sup> give following values:

$$K_1 = -13500 \text{ J/m}^3$$

$$K_2 = -2800 \text{ J/m}^3$$

Both values are for room temperature. The constants  $c$  have a non-linear temperature dependence which is different for both. The calculation of a total anisotropy budget makes only sense if it refers to a certain temperature. Note that  $K_1$  becomes zero at the isotropic point, *i.e.* 135 K, and below that it becomes positive.

### 3. Surface anisotropy

In order to estimate a value of the surface anisotropy first an approach is followed which relies on the internal demagnetizing field distribution of a uniform cube which is inhomogeneous due to shape<sup>9</sup>.

Albeit the average demagnetization factor of a cube (like for a sphere) is  $N_{ave} = 1/3$ , the demagnetization factor near the cube faces and edges is considerably different from 1/3. Dunlop *et al.*<sup>9</sup> have calculated the demagnetization factors in inside a uniform cube. Figure 4 in ref<sup>9</sup> shows characteristic demagnetization factor profiles.

The maximal  $N$  appears at the center of the surface plane perpendicular to  $M_s$ . The smallest occurs at the edge of surface plane parallel to  $M_s$ . Using this difference, one can calculate a surface anisotropy constant caused by shape effects of the cube:

$$K_{ss}^V = \frac{1}{2} 4\pi \cdot 10^{-7} (0.52049 - 0.17572) (480 \cdot 10^3)^2 \frac{Vs}{Am} \frac{A^2}{m^2}$$

$$K_{ss}^V = 49910 \frac{Vs}{m} \frac{A}{m^2} = 49910 \frac{J}{m^3}$$

As this value refers to the volume, one has to revert it into a surface value, *i.e.* dividing by the surface to volume ratio. For cuboids with width  $w$ , length  $l$ , and depth  $d = w$  the above  $K_{ss}$  becomes:

$$K_{ss} = K_{ss}^V \frac{1}{2 \left( \frac{2}{w} + \frac{1}{l} \right)}$$

and with  $w = 18.6 \text{ nm}$  and  $l = 23.3 \text{ nm}$ :

$$K_{ss} = 49910 \frac{1}{2 \left( \frac{2}{18.6 \times 10^{-9}} + \frac{1}{23.3 \times 10^{-9}} \right)} \frac{J}{m^3} m$$

$$K_{ss} = 1.658 \times 10^{-4} \frac{J}{m^2}$$

This calculation of  $K_s$  is for a uniform cube, but for octopods the center of each surface is dented towards the nanoparticle center. For not too strongly deformed cubes, such as the synthesized octopods are, it is reasonable to assume that the difference between the maximal and the minimal  $N$  is similar to that of the uniform cube, but with the difference that the  $N$  profiles in Fig. 4 of ref.<sup>8</sup> have a more pronounced curvature. However, the surface anisotropy of nanoparticles is not only related to shape effects but is also caused by effects such as broken bonds, charge transfer, oxidation and reduced crystalline symmetry. As it is difficult to separate these different effects, surface anisotropy constants of MNPs are generally experimentally derived from the effective anisotropy constant via blocking temperature or ferromagnetic resonance measurements. According to Bødker *et al.*<sup>10</sup>, the effective volume anisotropy is:

$$K_{eff}V = K_vV + K_sS \quad \leadsto \quad K_{eff} = K_v + \frac{S}{V}K_s$$

with  $V$  and  $S$  being volume and surface, respectively. For cuboids with three different space dimensions, *i.e.* width  $w$ , length  $l$ , and depth  $d$ , the formula above becomes:

$$K_{eff} = K_v + 2 \left( \frac{1}{w} + \frac{1}{l} + \frac{1}{d} \right) K_s$$

Assuming that we can approximate the octopods with cuboids and that  $w$  equals  $d$ , the formula for  $K_{eff}$  simplifies to:

$$K_{eff} = K_v + 2\left(\frac{2}{w} + \frac{1}{l}\right)K_s$$

The ZFC/FC measurements of the octopods (Fig. 13a in the main manuscript) show that the blocking temperature  $T_B$  is at or above room temperature. Assuming a  $T_B$  of 300 K, the effective anisotropy would calculate as follows:

$$K_{eff} = \frac{T_B 25 k_B}{V} = \frac{T_B 25 k_B}{w^2 l}$$

$$K_{eff} = \frac{300 \cdot 25 \cdot 1.38 \times 10^{-23}}{(18.6 \times 10^{-9})^2 \cdot 23.3 \times 10^{-9}} \frac{K}{m^3} = 12840 \frac{J}{m^3}$$

$K_s$  can then be calculated, with  $K_v = K_l$ :

$$K_s = \frac{K_{eff} - K_1}{2\left(\frac{2}{w} + \frac{1}{l}\right)}$$

$$K_s = \frac{12840 - (-13500)}{2\left(\frac{2}{18.6 \times 10^{-9}} + \frac{1}{23.3 \times 10^{-9}}\right)} \frac{J}{m^3} = 8.8 \times 10^{-5} \frac{J}{m^2}$$

Which accounts for about the half of the shape-induced surface anisotropy.

#### 4. Total anisotropy

The total anisotropy  $K_{tot}$  at room temperature would be:

$$K_{tot} = K_1 + 2\left(\frac{2}{w} + \frac{1}{l}\right)(K_s + K_{ss}) + K_{us}$$

$$K_{tot} = -13500 \frac{J}{m^3} + 2\left(\frac{2}{18.6 \times 10^{-9} m} + \frac{1}{23.3 \times 10^{-9} m}\right)\left(8.8 \times 10^{-5} \frac{J}{m^2} + 1.658 \times 10^{-4} \frac{J}{m^2}\right) + 15866 \frac{J}{m^3}$$

$$K_{tot} = 78732 \frac{J}{m^3}$$

Here it is assumed that all anisotropic effects are along the same axis, i.e. the easy magnetization axis.

Note that below 160 K the total anisotropy constant, because:

$K_1$  becomes larger even zero or positive;

$K_{ss}$  and  $K_{us}$  increase due to the temperature dependence of the saturation magnetization.

**Dynamic Light Scattering (DLS) measurements.** After the grafting step, the colloidal stability in water has been evaluated by Dynamic Light Scattering (DLS) (Figure S11). Results on dendronized IONPs with the highest IONP size are given here. Dendronized NS22 presented no sign of aggregation with a monomodal hydrodynamic size distribution centred at about 28 nm, larger than the TEM size of NPs of about 22 nm which may be attributed to the dendron coating and solvation layer.

For octopod-shaped NPs, this measurement is an indication of a possible aggregation but cannot be considered as a precise measurement of the hydrodynamic diameter. The optical model used to calculate the size distribution considered spherical NPs. Anisotropic NO28 may be present in front of the laser under different orientations that can be longer than the edge length or the diameter. Therefore, the values of hydrodynamic diameter are just given for comparison and cannot be considered as relevant. Dendronized NO28 presented a monomodal distribution in water centred at 32 nm. In conclusion, dendronized NPs display an average hydrodynamic diameter smaller than 100 nm.

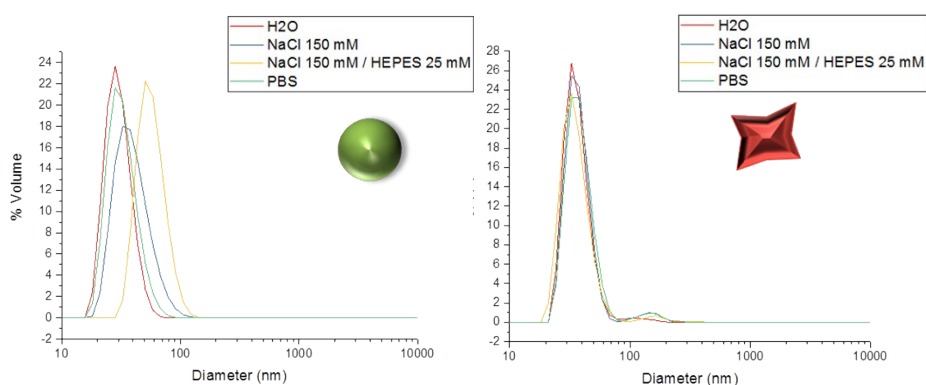


**Figure S12.** DLS measurements of samples NS22 and NO28 in different physiological media.

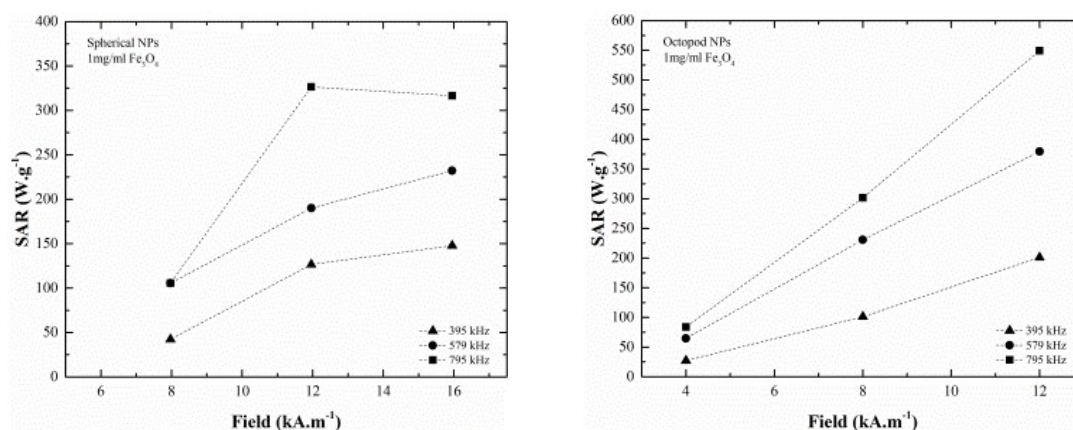


**Figure S13.** SAR values for spherical NS18 and octopod NO18 NPs measured at 1 mg/ml in aqueous suspension. No significant heat loss was measured for spherical NPs at 4 kA·m<sup>-1</sup>. Data for NO18 at 16 kA·m<sup>-1</sup> could not be fitted as evaporation was too important due to the high temperature achieved.

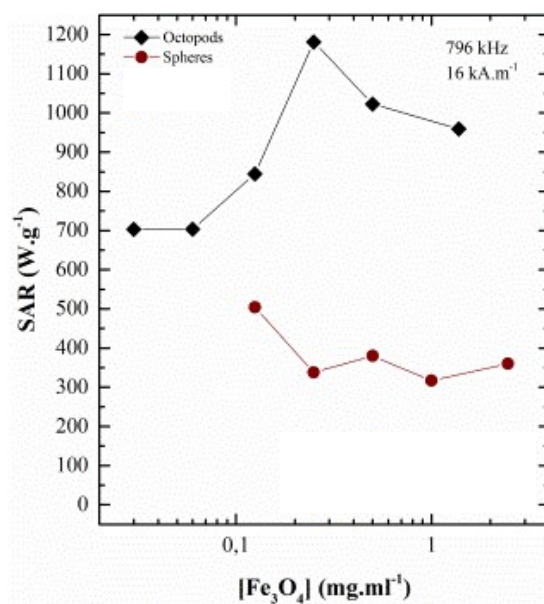


**Figure S14.** SAR values for spherical NS18 and octopod NO18 NPs measured as decreasing concentration from 1 mg/ml in aqueous suspension measured at 796 kHz and 16 kA·m<sup>-1</sup>. SAR value for NO18 at 1 g·l<sup>-1</sup> may not be accurate as evaporation occurred due to the elevated temperature.

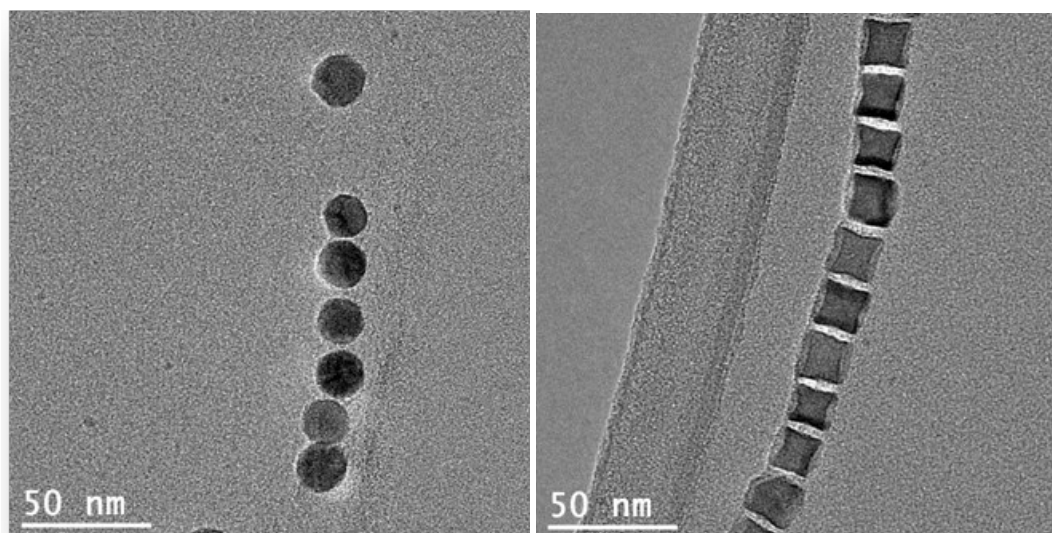


**Figure S15.** TEM images of nanospheres (left) and octopods (right) showing a spontaneous alignment upon deposition on TEM grids.

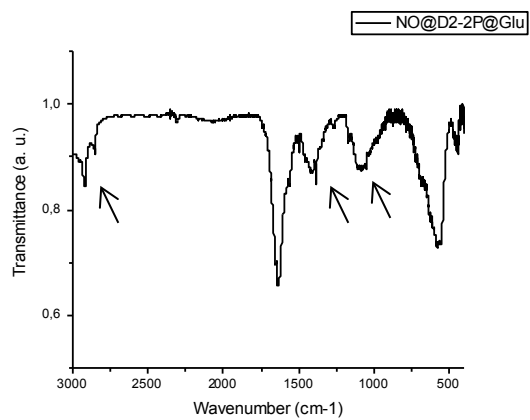


**Figure S16.** IR spectra of dendronized NO28 after the coupling of glucose (arrows: IR bands of glucose).

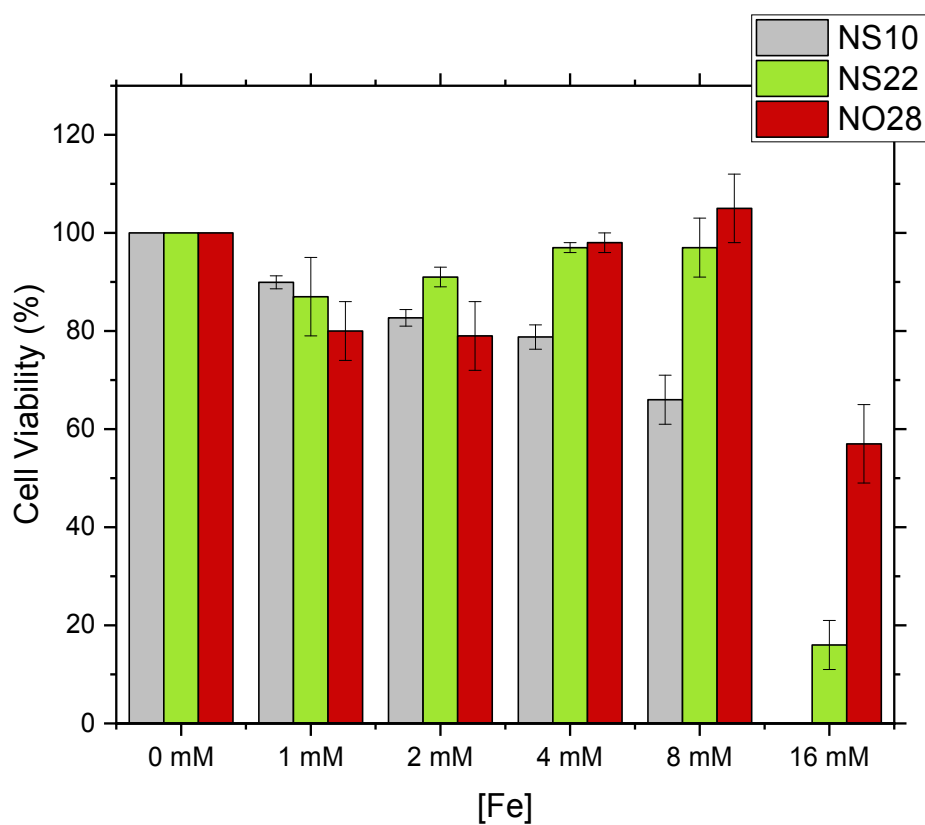


**Figure S17.** Cell viability of Huh-7 cell monolayer as a function of the NPs shapes, 10 nm spheres (NS10: grey), NS22 (green) and NO28 (red)

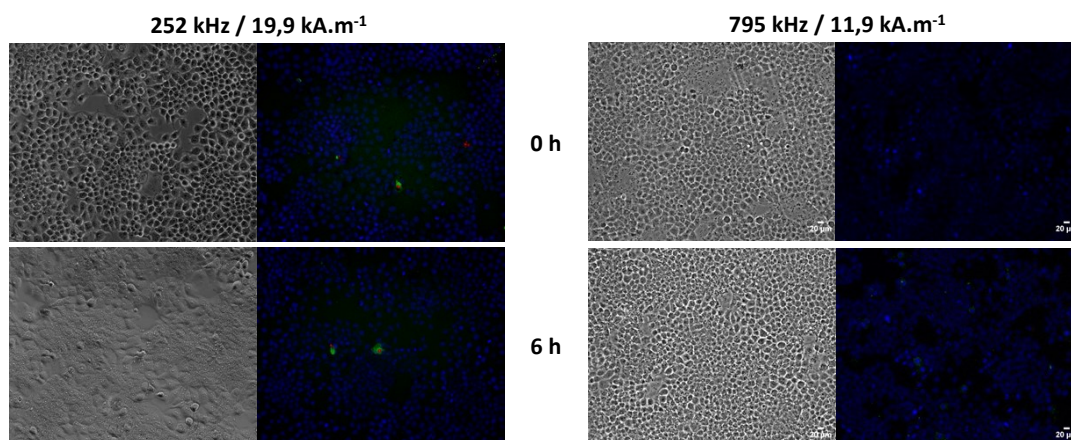


**Figure S18.** Control experiments on Huh-7 cells without loaded NPs. Cells were labeled with Annexin V-FITC (green), PI (red) and hoechst (blue).

To further check the *in vivo* magnetic hyperthermia properties of dendronized octopods NO28, they have been injected intratumorally in mice. After having performed the experiments detailed in experimental part, the tumor growth was calculated as (Tumor Volume)/(Initial Tumor Volume) and is given in Figure S18. Day 2 corresponds, as can be seen in the experimental design scheme 1, to the measurements made after the last of the three MH treatment days. Day 4 corresponds to the measurements made 48h after the last MH treatment. The different experimental conditions were:

BH: 4 mice with the tumor, without MNPs and with magnetic field exposure

BNPs: 3 mice with the tumor, with MNPs and without magnetic field exposure

HNPs: 3 mice with the tumor, with MNPs and with magnetic field exposure.

At day 4, two of the mice of the HNPs group and 1 of the BNPs group had to be sacrificed because of tumor ulceration. Although tumor volumes were not too large, this ulceration takes place because skin stretching cannot match tumor growth rate.

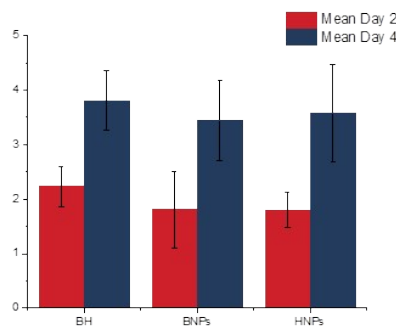


**Figure S19a.** Evolution of tumor growth in conditions detailed above.

PERLS staining was performed in order to detect NPs in images from tissue sections (Figure S18b-c). It can be seen that NPs are mainly in the extracellular matrix, but some can be detected in the tumor. However, no effects in tumor inhibition growth have been detected in mice with NPs after AMF exposure. NO28 NPs were very stable and easy to inject, but the main problem is that they stayed in the extracellular matrix instead of being internalized in the tumor.

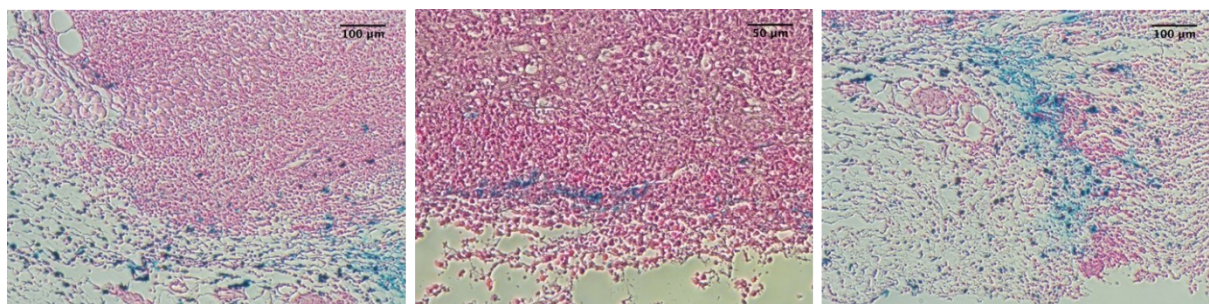


**Figure S19b.** PERLS images of tumors of the group BNPS (with NPs without AMF)

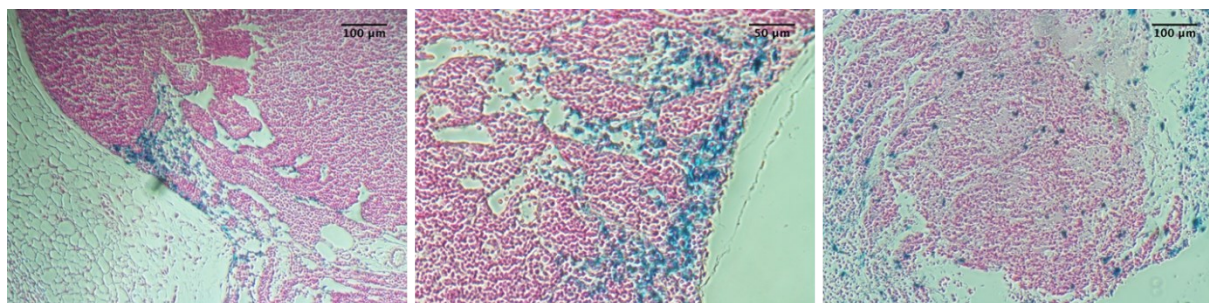


**Figure S19c.** PERLS images from tumors of the group HNPS (with NPs with AMF)

## References

- 1 B. Basly, G. Popa, S. Fleutot, B. P. Pichon, A. Garofalo, C. Ghobril, C. Billotey, A. Berniard, P. Bonazza, H. Martinez, D. Felder-Flesch and S. Begin-Colin, *Dalton Trans.*, 2013, **42**, 2146–2157.
- 2 G. Lamanna, M. Kueny-Stotz, H. Mamlouk-Chaouachi, C. Ghobril, B. Basly, A. Bertin, I. Miladi, C. Billotey, G. Pourroy, S. Begin-Colin and D. Felder-Flesch, *Biomaterials*, 2011, **32**, 8562–8573.
- 3 B. Basly, D. Felder-Flesch, P. Perriat, C. Billotey, J. Taleb, G. Pourroy and S. Begin-Colin, *Chem. Commun.*, 2010, **46**, 985–987.
- 4 T. J. Daou, S. Begin-Colin, J. M. Grenèche, F. Thomas, A. Derory, P. Bernhardt, P. Legaré and G. Pourroy, *Chem. Mater.*, 2007, **19**, 4494–4505.
- 5 L. Polito, M. Colombo, D. Monti, S. Melato, E. Caneva and D. Prospero, *Journal of the American Chemical Society*, 2008, **130**, 12712–12724.
- 6 J. L. Dormann, D. Fiorani and E. Tronc, in *Advances in Chemical Physics*, eds. I. Prigogine and S. A. Rice, John Wiley & Sons, Inc., 1997, pp. 283–494.
- 7 D. J. Dunlop and Ö. Özdemir, *Rock Magnetism: Fundamentals and Frontiers*, Cambridge University Press, 2001.
- 8 R. Prozorov and V. G. Kogan, *Phys. Rev. Applied*, 2018, **10**, 014030.
- 9 D. J. Dunlop, R. J. Enkin and E. Tjan, *Journal of Geophysical Research: Solid Earth*, 1990, **95**, 4561–4577.
- 10 null Bodker, null Morup and null Linderöth, *Phys. Rev. Lett.*, 1994, **72**, 282–285.